International Journal of Biological Macromolecules 329 (2025) 147809

Contents lists available at ScienceDirect

International Journal of Biological Macromolecules

journal homepage: www.elsevier.com/locate/ijbiomac

Surface functionalization with short PAS-sequence affects H-ferritin nanocage stability

Ilaria Tagliolini [a,1], Francesca Gorgoglione [a,1], Marta Sevieri [a], Beatrice Bignami [a], Valeria Giacobbo [a], Claudia Pigliacelli [b], Francesca Baldelli Bombelli [b], Fabio Corsi [a,c], Renata Tisi [d,*], Serena Mazzucchelli [a,*]

[a] Dipartimento di Scienze Biomediche e Cliniche, Università degli studi di Milano, 20157, Milano, Italy
[b] Dipartimento di Chimica, Materiali, ed ingegneria chimica "Giulio Natta", Politecnico di Milano, Milano, 20131, Italy
[c] Istituti Clinici Scientifici Maugeri IRCCS, via Maugeri 4, 27100, Pavia, Italy
[d] Dipartimento di Biotecnologie e Bioscienze, Università di Milano-Bicocca, 20126, Milano, Italy

ARTICLE INFO

Keywords:
H-ferritin nanocages
PASylation
Nanodrug delivery system

ABSTRACT

H-ferritin nanocages (HFn) are promising tumor-targeting delivery systems owing to their specificity and reduced off-target toxicity. However, their short half-life and rapid clearance currently limit clinical application. PASylation has been used to increase the *in vivo* half-life of HFn, without introducing negative effects. To date, all knowledge is limited to PASylated HFn containing PAS domains of 40 and 75 amino acids. Herein, we investigate the impact of shorter PAS domains on the stability of HFn, focusing on a mutant modified with 20 amino acids PAS domains. PAS20-HFn monomers were successfully produced and purified but seems unable to form stable quaternary structure. To investigate this, we studied the structural dynamics properties of native HFn, PAS20-HFn, PAS40-HFn dimers, tetramers, and octamers. Our simulations indicate that PAS20-HFn tetramers exhibit increased flexibility in a region encompassing the end of the D helix, the D-E turn and the beginning of the E helix. This flexibility is critical for dimer interactions and facilitates the subsequent organization of higher-order complexes. During the folding of PAS20-HFn octamers, PAS domain disrupts the proper association of the C-terminal *E*-helices, leading to instability in the nanocages. This highlights the bipolar and essential role of HFn PASylation in HFn nanocages, especially concerning their size.

1. Introduction

In the last twenty years, we witnessed the rise of cancer nanomedicine, aimed at developing nanosystems to specifically deliver anticancer agents in tumor [1]. Indeed, nanoparticle-based drug delivery systems enhance the physicochemical properties of anticancer agents to limit their off-target accumulation, reducing side effects and improving therapeutic efficacy [2]. Natural nanocages offer significant advantage over synthetic nanoparticles as they are nearly invisible to the immune system, exhibit excellent biocompatibility, and have minimal toxicity. Among them, H-Ferritin nanocages (HFn) hold promise as efficient tumor-targeted nanodelivery systems, given their unique features which include: (1) structurally homogeneous cage-like assembly of 12 nm, allowing precise control of the amount of encapsulated molecules; (2) stability in physiological environment; (3) capability to escape the Reticuloendothelial System, increasing accumulation to the target site; (4) suitability for surface engineering by chemical or genetic insertion of target functionalities to drive recognition of specific cell biomarkers or to modulate bioavailability and circulation time [3–8]; (5) natural tumor homing, mediated by the interaction with the transferrin receptor-1 (TfR1), which is overexpressed in most types of solid cancers, in relation to their aggressiveness [9–13]. HFn can specifically bind and be internalized in a panel of human and murine cancer cells [14–18], while *in vitro* interaction with healthy cells is negligible. This solution has already been tested for the encapsulation of various dyes and drugs, displaying optimal efficacy. In particular, the encapsulation of doxorubicin (DOX) and indocyanine green (ICG) has been extensively studied [14–16,18–20]. Despite the significant efficacy demonstrated *in vitro* in cancer Patient Derived Organoids (PDO), as well as murine models, and the pivotal role of this nanoformulation in mitigating DOX-

* Corresponding authors.
E-mail addresses: renata.tisi@unimib.it (R. Tisi), serena.mazzucchelli@unimi.it (S. Mazzucchelli).
[1] These authors contributed equally to the work.

https://doi.org/10.1016/j.ijbiomac.2025.147809
Received 15 July 2025; Received in revised form 11 September 2025; Accepted 18 September 2025
Available online 19 September 2025

induced T-cells toxicity [21,22], biodistribution studies have revealed some limitations. The natural HFn tumor homing due to TfR1-mediated uptake provides improved ICG tumor accumulation in comparison to free dye, accurate definition of the anatomic structures and precise tracking of tumors and metastasis. However, HFn@ICG (and also HFn in general) suffers suboptimal tumor to background (T/B) ratio due to HFn short circulation time and quick wash-out. Several engineering strategies have been proposed to modify HFn surface to increase nanocage's stability, improve bioavailability, biodistribution, circulation time and tumor accumulation [23]. Most of them are unable to preserve TfR1-mediated specific uptake. Alternatively, the introduction of a tumor metalloproteinase (MMP)-sheddable PAS domain, characterized by a sequence of proline, alanine and serine residues that form an unfolded domain resembling the polyethylene glycol shell, has been proposed as a promising strategy to increase circulation time and stability, while preserving tumor targeting [24,25]. Indeed, this selection of amino acids is based on specific characteristics that promote the formation of a random coil structure, effectively counteracting the natural tendency to develop secondary structural elements. As reported in literature, polymers of alanine fold into α-helical structures, serine polymers create β-sheet structures, while proline polymers typically form type II trans helices [26]. Several studies have proposed the development of PASylated ferritin mutants with PAS domain of 40 and 75 amino acids, respectively. These PAS sequences were selected to achieve a nanocage with hydrodynamic size not exceeding 20 nm. Indeed, size adjustments were initially achieved by designing PAS chains with an extended conformation, followed by modification of the phi (Φ) and psi (Ψ) dihedral angles of alanine and serine residues in the regions allowed by the Ramachandran plot. Recombinant mutants produced in *E. coli* were encapsulated with DOX and compared with native HFn, displaying higher encapsulation. Moreover, a significant improvement *in vivo* circulation times was observed with PASylated HFn [26,27]. Currently, there are no studies in literature regarding PAS domains shorter than 40 amino acids. For this reason, we decided to study the HFn mutant, PAS20-HFn, which comprises a 20-aminoacid PAS domain, and evaluate its features in comparison to the PAS40-HFn mutant, as well as the impact of a shorter PAS sequence. To date, there has been little published regarding the impact of very short PAS sequences on protein folding and functionality, and no information about the critical size of PAS sequences in HFn has been available until now [24,25,27,28]. In particular, here we propose to study how surface functionalization with a short PAS sequence affects HFn nanocage stability.

2. Materials and methods

2.1. Design of PAS20-HFn and PAS40-HFn

The cDNA encoding for PAS20-HFn and PAS40-HFn were designed in order to insert a PAS sequence, rich in proline, alanine and serine, of 20 (ASPAAPAPASPAAPAPSAPA) and 40 (ASPAAPAPASPAAPAPSAPAASPAAPAPASPAAPAPSAPA) amino acids respectively, at the N-terminal end of the HFn aminoacidic sequence. Between PAS sequences and HFn has been inserted a consensus sequence (PAS_GGGPLGLAGGGG_HFn) responsive to proteolytic cleavage by different metalloproteinases (MMPs). cDNAs with the designed sequences were synthesized and subcloned into the vector pET11a by Genescript, obtaining the plasmids pET11a/PAS20/MMPs/HFn and pET11a/PAS40/MMPs/HFn.

2.2. Production of PAS20-HFn and PAS40-HFn

The resulting plasmids were used to transform *E. coli* strain BL21 (DE3) using the heat-shock method. The transformation procedure was carried out simultaneously for PAS20-HFn and PAS40-HFn, adding 10 ng of each plasmid DNA to 200 μL of BL21(DE3) cells. The growth of the transformed strains happened at 37 °C in Luria Bertani medium composed of yeast extract, tryptone, sodium chloride 170 mM and D-glucose 5.5 mM with ampicillin 100 μg/mL until OD (Optical density) 600 nm = 0.6. To determine the optimal induction parameters, we tested different concentrations (0.5 and 1 mM) of isopropyl β-D-1-tiogalactopiranoside at various incubation times. After the induction tests, we chose 0.5 mM as the suitable concentration to induce the production of PAS20-HFn (after 24 h) and PAS40-HFn (after 4 h) in bacteria cells. At the end of the induction time, the cells were collected and centrifuged for 15 min at 4000 ×*g*, at 4 °C. The pellet was resuspended in phosphate-buffered saline buffer and centrifuged under the same conditions. The resulting pellets were washed and resuspended in lysis buffer (3 mL/g of cells; Tris-HCl 20 mM pH 8.00, PMSF 1 mM, protease inhibitors complete EDTA-free 1 mM, lysozyme 1 mg/mL, $MgCl_2$ 20 mM. Subsequently, deoxyribonuclease I from bovine pancreas (40 U/g of cells) was added to the solution and incubated at 4 °C in ice for 30 min. To obtain the crude extract (CE), the solution was sonicated for 6 cycles of 10 s applying an ultrasonic output of 50 W in an ice bath and centrifuged at 10.000 ×*g* for 30 min at 4 °C. The crude extract was incubated with DNase 0.1 mg/mL for 1 h at 37 °C in a thermostatic bath and subsequently heated for 15 min at 70 °C and centrifuged under the same conditions as the previous centrifugation step. The heat-treated (HT) was ultracentrifuged using Optima MAX Ultracentrifuge for 1 h at 35.000 rpm, 4 °C. To precipitate the mutants, PAS20-HFn and PAS40-HFn, the supernatant was incubated with ammonium sulfate at 65 % (*w/v*) for 2 h. After incubation, the solution was centrifuged under the same parameters as before, and the pellet was resuspended in Tris-HCl 20 mM pH 8.00. The solution was dialyzed overnight at 4 °C to remove excess ammonium sulfate. The following day, the buffer was changed again and after 2 h, the final solution (PD fraction) was collected and further purified by chromatography.

2.3. Ion exchange chromatography (IEC)

Purification was performed using strong ion exchange chromatography (IEC) in which the resin HiTrap Q Sepharose High Performance (cat# GE Healthcare) and Tris-HCl 20 mM pH 8.00 buffer were used. The resin was packed in a 1.0 × 10 cm column (2 mL bed volume) to separate proteins according to their charge. After washing and equilibrating the column with MilliQ water and Tris-HCl 20 mM pH 8.00 respectively, the dialyzed supernatant was loaded into the column and seven fractions (E, F1, F2, F3, F4, F5, F6) of four milliliters each were collected. Elution was performed with a stepwise gradient of NaCl (0.1–0.5 M) in Tris-HCl 20 mM pH 8.00. In detail, E was collected after loading the dialyzed heat treated, then another volume of Tris-HCl 20 mM pH 8.00 was used to collect F1. Fractions from 2 (F2) to 6 (F6) were collected using 20 mM Tris-HCl pH 8.00 supplemented with a discontinued NaCl gradient from 0.1 M to 0.5 M. PAS20-HFn was also purified using a weak anion exchange chromatography resin, DEAE-Sepharose (cat# DFF100, Sigma-Aldrich). A column with a bed volume of 2 mL was used for weak anion exchange chromatography. The sample was dialyzed in 20 mM KMES pH 6.0 and loaded into the column, collecting the excluded fraction. Then, the column was washed with 5 volumes of KMES 20 mM pH 6.0 and the six fractions with purified protein were collected using KMES 20 mM pH 6.0 with a stepwise NaCl gradient, from 70 mM to 420 mM.

2.4. Size exclusion chromatography (SEC)

For Size Exclusion Chromatography, the fast protein liquid chromatography system (FPLC NGC 10 Bio-Rad) was coupled with the ENrich 650 gel-filtration column (Bio-Rad) equilibrated with PBS. For purification purposes, a volume of 800 μL of dialyzed heat-treated sample obtained as previously described was injected into the loading loop (1 mL) and loaded onto the column. To characterize the purified PASylated HFn variant a volume of 200 μL of PAS20-HFn or PAS40-HFn was injected into the loading loop (1 mL) and loaded into the Superose6

10/300 GL column. The FPLC system operated at a flow rate of 0.5 mL/min with a maximum pressure of 600 psi. Fractions of 0.5 mL were collected by monitoring the chromatogram from the integrated ChromLab Software (Bio-Rad).

2.5. Characterization of PAS20-HFn and PAS40-HFn

PAS20-HFn and PAS40-HFn collected fractions were quantified employing NanoDrop 2000c (Thermo Fisher Scientific) by 280 nm absorbance (A280) and Pierce™ Bradford Plus Protein Assay Reagent (Thermo Fisher), according to manufacturing specifications. Proteins were analyzed using 12 % (*w/v*) SDS-PAGE polyacrylamide gels, running at constant voltage of 80 V and labelled with Coomassie stain (Imperial protein stain). To evaluate the morphology of the nanocages and examine their structural integrity Transmission Electron Microscopy (TEM) has been performed. A 20 μL drop of suspension was spotted on the Formvar grid and left to dry at RT, stained with uranyl-acetate 1 % for 30 s and dried overnight at RT. The following day, they were analyzed using TEM (Tecnai Spirit, FEI, Hillsboro, OR, USA) and images acquired at 80.000–300.000× magnification. Dynamic Light Scattering (DLS) was performed to study the size and the size distribution profile of the nanocages in a suspension. The measurements were performed using Zetasizer Nano Instrument (Malvern Panalytical). The analysis was conducted with a scattering angle of 173°, at 25 °C and each measurement was composed of 3 runs of 10 s. 1 mL of sample, previously diluted, filtered in distilled water, and equilibrated for 30 s to optimize conditions and minimize interference, was placed in a disposable cuvette (optical path length: 1 cm). All final hydrodynamic size distributions (intensity-weighted) of the samples studied were delivered by fitting autocorrelation functions using CONTIN algorithm. Circular Dichroism (CD) analysis was conducted to examine the secondary structure contents of the mutants (α-helices, β-sheets and random coils). The CD analysis was carried out in PBS buffer, after subtracting the buffer background signal in a 0.1 cm quartz cuvette using a J-815 CD spectrometer (Jasco). The experiments were run in a wavelength range between 190 and 350 nm with a data interval of 0.1 nm. The accumulation was adjusted to 10, sensitivity was set to standard, scanning speed to 100 nm/min, bandwidth to 1.00 nm, and Integration Time to 0.5 s. The recorded spectra were then smoothed to improve data quality and readability. Finally, secondary structure content was evaluated using the DichroWeb online server, employing the CONTIN-LL algorithm together with the SP175t reference set. The analysis provided the relative proportions of structural elements, specifically helix1 (regular α-helix), helix2 (distorted α-helix), strand1 (regular β-sheet), strand2 (distorted β-sheet), turns, and unordered regions. CONTIN-LL yielded two types of results: the closest matching solution across all proteins, and the average of all matching solutions. In accordance with the recommendation by Miles et al., the first dataset was selected for reporting [29].

2.6. Computational studies

To investigate the structural characteristics of PAS20-HFn and PAS40-HFn, we performed protein structure modelling using Alpha Fold3 (AF3) server (https://alphafoldserver.com/). AF3 was used to generate five 3D structural models of native HFn, PAS20-HFn, and PAS40-HFn dimers, tetramers, and octamers, entering the amino acids FASTA sequence of the protein as the only input. The models predicted were accompanied by the Expected Position Error graph, representing the position-wise error estimate (EPE) and the predicted local distance difference test (pLDDT), or per-residue measure of local confidence (Fig. S6 reports the quality assessment for the octamers, where the single monomers assessment can also be appreciated). The pLDDT provided a score above 90 (very confident) for the structure corresponding to the native ferritin, but very low (below 50) for the PAS modifications, as it is expected due to their disordered properties (Figs. 6A and S6E). The software also provided the pTM score, which was also linked to the confidence of the models, and the ipTM score which gives a measure of the confidence of the interaction surface in the models. Values of pTM > 0.6 and ipTM >0.8 indicated a high confidence in the predicted models.

2.7. Coarse-grain molecular dynamics simulations

Single-trajectory canonical molecular dynamics (MD) simulations of protein dynamics were performed by using the coarse-grained (CG) UNRES model on the UNRES server (version 23.01.2025) (https://unres-server.chem.ug.edu.pl////) [30,31]. The CG-MD simulations were performed in the NEWCT-9P UNRES force field with simulation steps of 48,9 fs, with five replicas with each one of the models generated from AF3 server for native HFn, PAS20-HFn, and PAS40-HFn dimers and tetramers as a starting point, for a minimal time of simulation of 40 ns each. The octamers simulations were performed as two replicas for each system, for a simulation time of minimum 25 ns for each replica, according to the limit of calculation time allocated by the server. The RMSD graph showed that a plateau was reached within 10 ns of simulation for all of the replicas. The radius of gyration also indicated a rapid change within the first 10 ns of simulation and remained stable ever after (see Figs. S8, S9, S10).

Videos of the trajectory were generated in PyMOL software, aligning the Cα items of the structures in the single 0.0489 ns-frames in order to reduce translational motions. A 5-frames window average of coordinate states was used to suppress high-frequency vibrations in the molecular dynamics-trajectory.

2.8. Model visualization and structural overlay

The visualization of the predicted molecules and their overlay was performed using various 3D graphics software such as PyMOL or ChimeraX. Videos of the molecular dynamics trajectories were produced with PyMOL.

2.9. PAS cleavage assessment

To evaluate the matrix metalloproteinase (MMP)-mediated removal of the PAS40 and PAS20 sequences from PAS40-HFn and PAS20-HFn, an enzymatic cleavage assay was carried out using collagenase I from *Clostridium histolyticum* (Sigma-Aldrich).

PAS40-HFn was incubated with collagenase I at a 1:4 M ratio (Collagenase I:PAS40-HFn) at 37 °C in a shaking incubator (Model 3032, GFL), while PAS20-HFn was incubated at the molar ratio 1:1. Aliquots were collected at different time points (5 min, 15 min, 1 h, and 2 h for PAS40-HFn, while 1, 2, 3, 4, 24, 72, 96 and 120 h for PAS20-HFn). Cleavage has also been performed also on PAS20-HFn monomers. Samples were analyzed by SDS-PAGE using a 12 % (*v*/v) polyacrylamide gel stained with Coomassie Brilliant Blue.

2.10. Binding assay

An *in vitro* Cell Binding Assay was performed at 4 °C to estimate the capability of PAS40-HFn and PAS20-HFn nanocages to bind to 4 T1-murine cells in comparison to HFn. 2×10^5 cells/tube were collected and incubated for 2 h at 4 °C in a blocking buffer (PBS + 0,3 % BSA) supplemented with 100 μg/mL of FITC-labelled nanocages. PAS40-HFn-F and PAS20-HFn-F were tested before and after cleavage. For each condition, 2 replicates were prepared. At the end of incubation, cells were washed 3 times with PBS, resuspended in 0.5 mL of PBS, and analyzed using a CytoFLEX flow cytometer (Beckman Coulter). For each analysis, 20,000 events were acquired after gating on viable cells and singlets. The proper gates were adjusted using a sample of untreated cells.

2.11. ICG loading and dye quantification

To obtain ICG-loaded PAS40-HFn, PAS40-HFn and HFn, the pH-triggered loading procedure has been employed [11,16,20,21]. Briefly, a mixture of HFn nanocages (0.5 mg/mL) was dissolved in NaCl 0.15 M and led to pH 2.0 to unfold the nanocage. After a 15-min incubation at RT under stirring, the pH was then brought to 7 and ICG powder Verdye (25 mg; Diagnostic Green GmbH, Germany), previously solubilized in distilled deionized water (5 mg/mL), was added to the mixture at a final dye concentration of 1 mg/mL. The pH was then returned to neutrality (pH 7.5) and the solution was incubated for 2 h at RT and under 180 rpm shaking to completely achieve the refolding of the quaternary structure. The resulting PAS40-HFn@ICG, PAS20-HFn@ICG and HFn@ICG were concentrated employing Amicon Ultra-4 centrifugal filter devices (4 mL, MWCO 100 kDa, Millipore), and the non-encapsulated ICG was removed by gel filtration through Zeba Spin Desalting column (2 mL; 7 K MWCO, Thermo Scientific). To quantify the amount of encapsulated ICG, it was extracted from the nanocages using acetonitrile (ACN) with a ratio of 1:10. The solution was centrifuged for 10 min at 13000 rpm at 4 °C (Heraeus FRESCO 17 Centrifuge, Thermo Scientific) recovering the supernatant. The supernatant was diluted in milk and ICG content was quantified by measuring the fluorescence of the ICG using a dye standard curve, as previously reported [11,16,20,21].

2.12. Statistical analysis

Statistical analyses were conducted using either two-way ANOVA and Student's *t*-test using the GraphPad Prism version 8.00 for Windows (GraphPad Software, USA). All tests assumed normal distribution. The statistical significance threshold was set at $p < 0.05$ and all data were expressed as the mean ± SD.

3. Results and discussion

3.1. Design and production of PASylated HFn nanocages

Our design strategy first aimed at inserting a nucleotide sequence encoding for the PAS domain (PAS20 and PAS40), containing one or two repetitions of ASPAAPAPASPAAPAPSAPA, upstream of the cDNA encoding for HFn primary structure, by DNA recombinant technology. Then, we inserted the PLGLAG consensus sequence of MMP between HFn and PAS domain, to allow the tumor-specific cleavage of PAS domains once HFns reach the slightly acidic tumor microenvironment. To gain insight inon the possible outcome of such a design, 3D models of the structures of both protein mutants were obtained by using the bioinformatic software AlphaFold3 (AF3). As shown in Fig. 1, the 3D models highlighted that the PAS domain should be correctly exposed on the external surface of HFn nanocages in both cases, according to folding predictions.

Starting from these premises, the as-designed PASylated variants of HFn were cloned into the pET-11a vector and used to transform the bacterial strain BL21(DE3). To assess the most appropriate induction parameters, different concentrations of inducer and different times of induction at 37 °C were evaluated. Considering the BL21(DE3)/pET11a/PAS20-HFn strain, the treatment with 0.5 mM IPTG for 24 h was selected as best condition to produce PAS20-HFn. In fact SDS-PAGE analysis of soluble fractions achieved after 0.5 mM IPTG induction showed the presence of a distinct band of about 25 kDa, as the induction time increases (Fig. S1A and S1B). In addition, we identified induction with IPTG 0.5 mM for 4 h as the optimal parameters for PAS40-HFn production, as evidenced by the increased intensity of the band at 27 kDa corresponding to PAS40-HFn (Fig. S2A and S2B).

3.2. PAS40-HFn purification and characterization

Bacterial growth of BL21(DE3)/pET11a/PAS40-HFn strain was performed according to the protocols described in Methods section (*Production of PAS20-HFn and PAS40-HFn*), resulting in a bacterial pellet of approximately 2.12 g/L of culture. The bacterial cells were lysed obtaining the crude extract (CE; Figs. S3 and 2A) and PAS40-HFn was purified using a multiple-step procedure achieving the HT and PD samples (Figs. S3 and 2A). After that, PAS40-HFn was purified by ion exchange chromatography (IEC) HiTrap MonoQ Sepharose High Performance, yielding an average of 13.89 ± 4.69 mg of protein per gram of bacterial pellet. The SDS-PAGE analysis revealed the presence of a signal at the expected molecular weight of 27 kDa for PAS40-HFn in the flow-through fraction, as well as in fractions 1, 2, and 3, with lesser amounts in the remaining fractions (Fig. S3A). Although this purification method produced a good amount of correctly folded protein, as confirmed by TEM image (Fig. S3B), the purity of the samples was inadequate due to the presence of multiple non-specific bands (Fig. S3). Therefore, size exclusion chromatography (SEC) was implemented as a purification strategy. The PD sample was loaded on the FPLC NGC system equipped with the ENrich 650 gel-filtration column and fractions from F9 to F11.5 were collected following the protein absorbance profile. Notably, the purified fractions analyzed by SDS-PAGE (Fig. 2A) were found to be highly pure, solely showing the presence of a band in correspondence to the expected MW of PAS40-HFn. We obtained a yield of 2.29 ± 1.04 mg of protein per gram of bacterial pellet (Table 1). Besides the preparative use of SEC, purified fractions of PAS40-HFn were loaded onto Superose 6

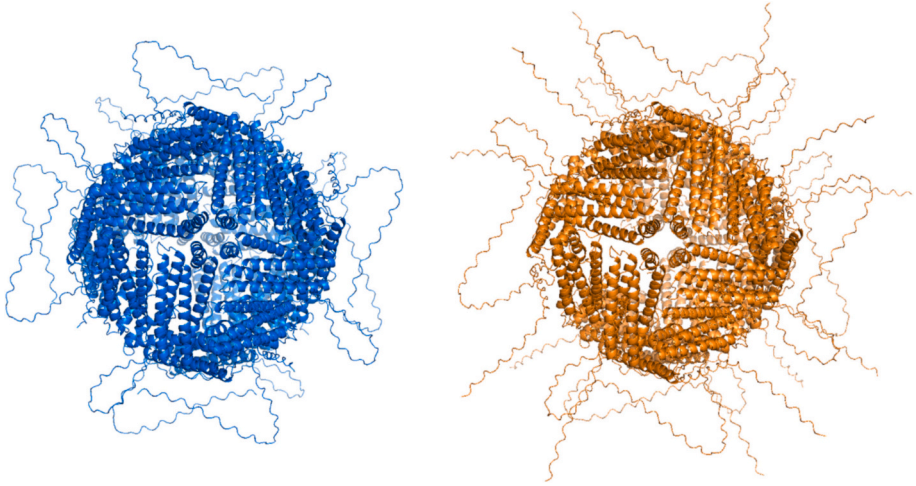

Fig. 1. 3D Models of the 2 mutants, PAS20-HFn (blue) and PAS40-HFn (orange), predicted by AlphaFold3 software.

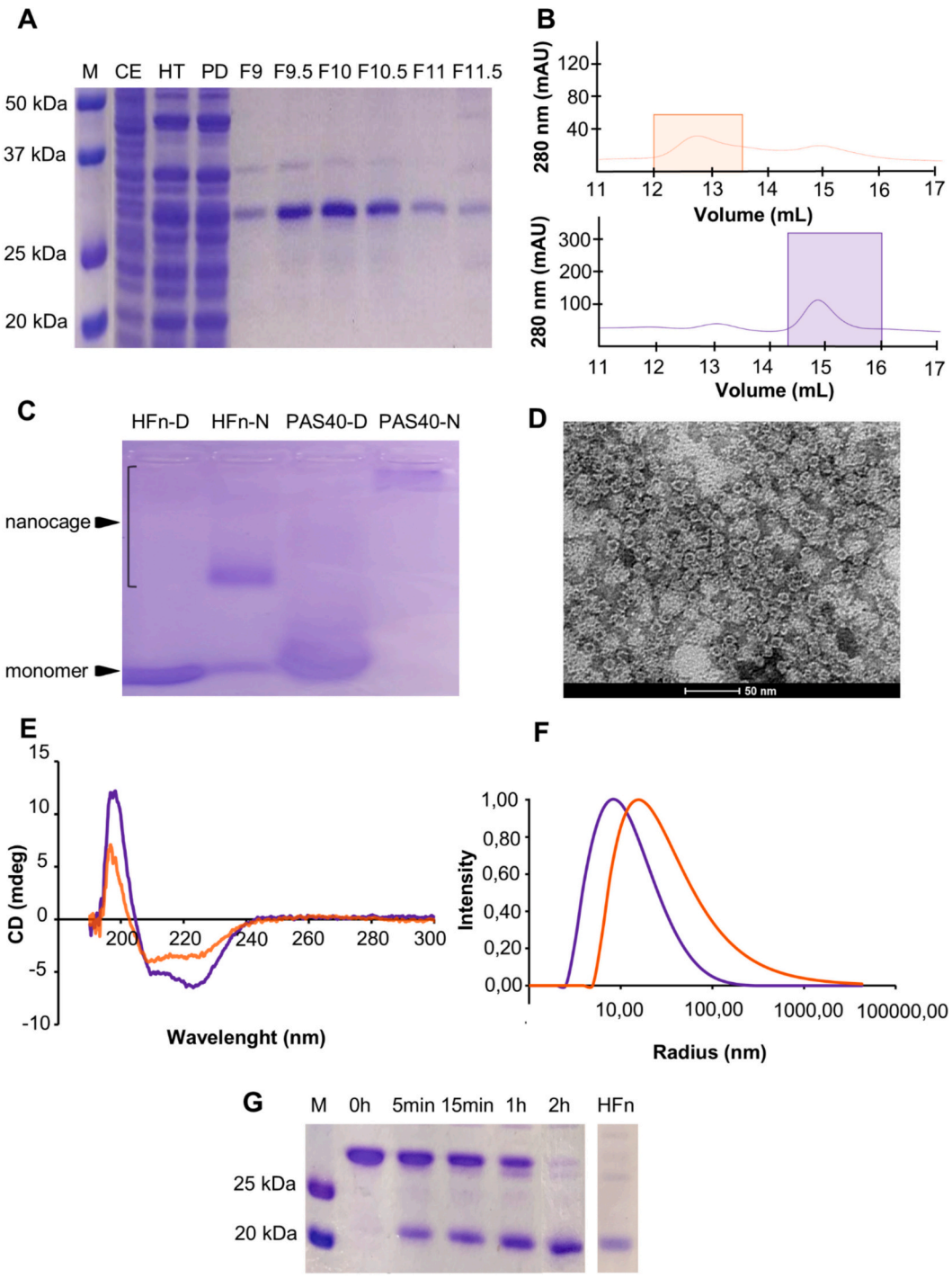

Fig. 2. PAS40-HFn characterization. A) SDS-PAGE 12 % (*v*/v) of PAS40-HFn purification. M = molecular size marker. Crude extract (CE), heat-treated (HT), dialyzed sample (PD), fraction (F). 12 μg of protein were loaded for CE, HT, PD whereas 4 μg of protein were loaded for F. B) Comparison between PAS40-HFn (orange) and HFn (violet) FPLC chromatograms obtained with Superose 6 10/300 GL column. C) Agarose gel characterization. Denatured HFn (HFn—D), non-denatured HFn (HFn—N), denatured PAS40-HFn (PAS40-D) and non-denatured PAS40-HFn (PAS40-N). 4 μg of each sample were loaded on 1.75 % agarose gel. D) TEM analysis of PAS40-HFn samples. E) CD analysis of PAS40-HFn (orange) and HFn (violet) F) Unweighted Hydrodynamic Size-distribution obtained by DLS analysis of PAS40-HFn (orange) and HFn (violet). G) SDS-PAGE analysis of PAS40 domain cleavage. PAS40-HFn loaded in a 12 % (v/v) SDS-PAGE stained with Coomassie blue at different times after Collagenase I incubation. M = molecular weight marker.

10/300 GL column in comparison to native HFn for analytical purposes. Results reported in Fig. 2B confirmed the difference in size between PAS40-HFn and HFn. Indeed, PAS40-HFn elutes earlier (approximately at 12 mL) than HFn (approximately at 14 mL). To further characterize PAS40-HFn by size, a purified fraction was loaded onto an agarose gel and compared with HFn (Fig. 2C). Each sample (HFn and PAS40-HFn) was analyzed either in denatured or non-denatured (native) conditions to observe differences in size between disassembled and assembled nanocages (Fig. 2C). As expected, due to the presence of the PAS40 sequence, PAS40-HFn presents a different migration behavior in the electric field compared to HFn in both monomeric and nanocage structures. Indeed, comparing the relative mobility of non-denatured

Table 1
Yield of PAS40-HFn purification following IEC and SEC procedures.

Samples	Total mg HFn protein/g bacterial pellet	Replicates	Statistical significance
PAS40-HFn IEC	13.89 ± 4.69	4	$p < 0.06$ (*t*-test)
PAS40-HFn SEC	2.29 ± 1.04	8	

samples of PAS40-HFn and HFn, we observe that the band corresponding to PAS40-HFn is positioned at higher height (low migration) compared to HFn (Fig. 2C). However, this methodology does not allow for achieving conclusive results and sufficient resolution to visualize it clearly. TEM analysis was conducted to assess size, spatial organization and morphology of PAS40-HFn (Fig. 2D), demonstrating that PAS40-HFn maintains the native HFn's ability to form a spherical, cage-like structure with a defined hollow core. Then, CD analysis has been performed to gain further information on the secondary structure content of PAS40-HFn. According to the literature's data, HFn secondary structure is mainly composed of α-helices, which gives rise to a characteristic CD spectrum with two negative peaks at 208 and 222 nm, as reported in Fig. 2E. CD spectra of PAS40-HFn revealed a shift in the first peak (around 210–220 nm) compared to HFn, which is attributable to an increase in random coil content, as expected as a result of the presence of unstructured PAS sequences (Fig. 2E; Table S1). DLS analysis (Fig. 2F)

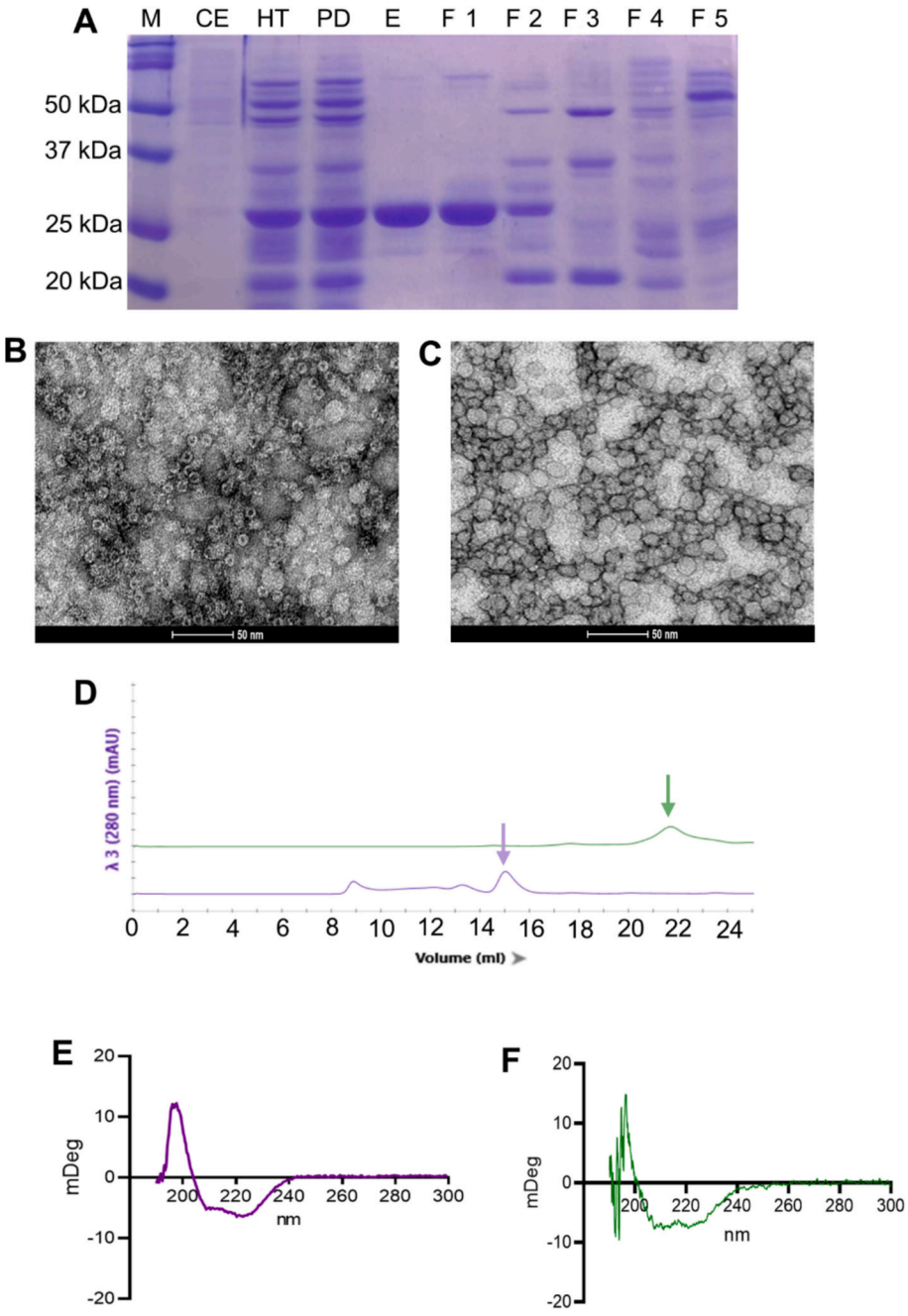

Fig. 3. PAS20-HFn characterization following Ion Exchange Chromatography. A) SDS-PAGE 12 % (*v*/v) characterization. M = molecular size marker. 12 μg of protein were loaded for CE, HT, PD, and excluded (E), whereas 4 μg of protein were loaded for fractions (F) 1–5. B) TEM analysis of native HFn and (C) of PAS20-HFn. D) Comparison between PAS20-HFn (green) and HFn (violet) FPLC chromatograms obtained with Superose6 10/300 GL column. E) CD analysis of HFn (purple) and PAS20-HFn (green).

revealed a slight increase in the hydrodynamic size with respect to HFn, likely due to the steric hindrance of the PAS shell. In addition, the presence of a single peak for each sample suggests the formation of a monodisperse population of nanocages in the solution with limited aggregation. Finally, to confirm the cleavage site functionality, we have incubated PAS40-HFn with collagenase I at 37 °C, observing a time-dependent release of the 20 kDa HFn monomer as a result of MMPs-mediated cleavage (Fig. 2G). These observations demonstrate that MMP cleavable sequences are not masked or made inaccessible by the presence of PAS sequences.

3.3. PAS20-HFn purification and characterization

Bacterial growth of BL21(DE3)/pET11a/PAS20-HFn strain was performed according to the protocols described in Methods section (*Production of PAS20-HFn and PAS40-HFn*). The bacterial cells (approximately 3.6 g/L of culture) were lysed and PAS20-HFn was purified using the multiple-step procedure already employed for PAS40-HFn. The heat-treated CE displayed an enrichment of the PAS20-HFn content (HT, Fig. 3A), while ammonium sulfate precipitation further improved its content and purity (PD, Fig. 3A). Then, PAS20-HFn has been purified by IEC using HiTrap MonoQ Sepharose High Performance. As already observed for PAS40-HFn, SDS-PAGE analysis of the PAS20-HFn purification process showed that, while the other proteins in the CE strongly interact with the MonoQ Sepharose matrix, PAS20-HFn was not bound, with pure fractions of PAS20-HFn in the excluded (E) and in fraction 1 (F1) (Fig. 3A). In contrast, progressively increasing the ionic strength of the elution buffer led to the eluition of other contaminant proteins alongside PAS20-HFn, resulting in impure fractions that were subsequently discarded (F 2–7; Fig. 3A). PAS20-HFn containing fractions (E and F1) were pooled together achieving a yield of 0.31 ± 0.01 mg of pure PAS20-HFn per gram of bacterial pellet and stored at −20 °C for further analysis (Table 2). The characterization of PAS20-HFn by TEM (Fig. 3C) in comparison to native HFn (Fig. 3B) proved the lack of a nanocage structure, suggesting that the PAS20 domain affects the capability of this mutant to fold into a quaternary structure. Chromatograms obtained by SEC of purified PAS20-HFn compared with that of native HFn strongly support this evidence (Fig. 3D) as PAS20-HFn eluted later than native HFn and in a position that strongly suggests a monomeric form. This data is strongly corroborated by the inability to characterize the sample by DLS, confirming the absence of nanocages in the solution (Fig. S4). Despite this, CD spectra of native HFn and PAS20-HFn (Table S1; Fig. 3E and F) revealed a similar content of secondary structure with the prevalence of α-helices. Moreover, in the PAS20-HFn spectra the unordered regions have been detected, as a result of the PAS20 domain presence, which is mostly constituted by random coil. To date, if we compare the amount of unordered region reported in Table S1 for PAS20-HFn *vs* HFn, we could observe something unexpected. Unordered content seems similar (0.183 *vs* 0.184), despite in the latter the unordered PAS domain is absent. Other interesting features observed in PAS20-HFn in comparison to HFn are the decrease of helix 1 component (0.230 *vs* 0.339) coupled with the increase in the helix 2 component (0.587 *vs* 0.345) (Table S1).

Table 2
Yield of PAS20-HFn purification following IEC and SEC procedures.

Samples	Total mg HFn protein/g bacterial pellet	Replicates	Statistical significance
PAS20-HFn IEC	0.31 ± 0.01	2	$p < 0.0005$ (*t*-test)
PAS20-HFn SEC	0.90 ± 0.31	10	

3.4. Evaluation of factors influencing PAS20-HFn nanocage stability

Starting from the unexpected observation that PAS40-HFn is able to form nanocages, while PAS20-HFn is not, we explored the potential reasons for this behavior. Firstly, we verified *E. coli* capability to produce correctly folded PAS20-HFn nanocages. To achieve this aim, we have analyzed the PAS20-HFn PD sample by TEM, indicating that at this purification step, PAS20-HFn nanocages could be detected (Fig. 4A). Despite this result denying our first hypothesis about *E. coli* inability to produce correctly folded PAS20-HFn able to stably form its quaternary structure, it suggests that the critical step affecting the nanocages stability occurs during chromatographic purification. We have thus identified two possible factors of the IEC procedure that could interfere with nanocage's folding: the ionic strength of the elution buffer (1) and the charge of the column matrix (2).

To exclude a negative impact of the ionic strength of the elution buffer, we set up different SEC purification runs with the same elution buffer used in the IEC process, Tris-HCl 20 mM at pH 8.0 pure or supplemented with NaCl 0.1 M, 0.2 M or 0.3 M. TEM images of purified fractions (Fig. 4B) clearly revealed the presence of functional PAS20-HFn nanocages. Moreover, SDS-PAGE analysis of pure fractions achieved by SEC highlighted a protein band at the foreseen molecular weight of 25 kDa. Unexpectedly, a signal at approximately double molecular weight (*i.e.* 50 kDa) has been detected (Fig. 4C), that could be attributed to PAS20-HFn dimers. In a nutshell, these results allowed us to exclude that the elution buffer negatively affects PAS20-HFn nanocages' stability.

Then, to assess the impact of the purification matrix in affecting PAS20-HFn nanocage stability, we replaced the monoQ Sepharose with DEAE-Sepharose, which is a much weaker anion exchanger. Indeed, both MonoQ and DEAE matrices are ion exchange chromatography resins, but they differ in their charge properties, binding mechanisms, and interacting amino acid residues. Mono Q Sepharose is a strong anion exchanger that exploits the quaternary ammonium ($–N^+(CH_3)_3$ as functional group. As a result, it is permanently positively charged. On the other hand, DEAE Sepharose is a weak anion exchanger, since its functional group is represented by Diethylaminoethyl ($–CH_2CH_2N(CH_2CH_3)_2$), which is positively charged only at pH < 9. As previously observed in Fig. 3, SDS-PAGE analysis of purified PAS20-HFn fractions (Fig. 4D) showed a strong signal at the expected molecular weight of PAS20-HFn monomers. However, TEM images displayed the lack of PAS20-HFn nanocages (Fig. 4E), strongly suggesting that, in these experimental conditions, the nanocages stability is affected resulting in quaternary structure folding issues. This evidence shows that the charge-charge interaction with the matrix may exacerbate structural instability of quaternary structure, as confirmed by the native agarose gel reported in Fig. S5.

To prove this, PAS20-HFn was purified using ENrich 650 gel-filtration column and characterized by Superose6 10/300 GL column. SEC chromatogram displayed an elution profile compatible with the presence of PAS20-HFn nanocages (Fig. 5A). SDS-PAGE analysis confirmed that the first eluted fractions contain PAS20-HFn, as demonstrated by the presence of a strong blue signal at the 25 kDa (Fig. 5B). Additionally, a strong signal at approximately double molecular weight (*i.e.* 50 kDa) has also been detected (Fig. 5B), as previously observed in Fig. 4E. TEM images acquired on PAS20-HFn purified by SEC (Fig. 5C) and compared with native HFn (Fig. 5D) highlighted that PAS20-HFn retains its quaternary cage-like structure with a defined hollow core. Results depicted in chromatograms reported in Fig. 5E confirmed the difference in nanocages' size between PAS20-HFn and HFn. Indeed, PAS20-HFn elutes approximately at 12 mL, a position consistent with the presence of its quaternary structure.

PAS20-HFn nanocages structure has also been confirmed by DLS analysis (Fig. 5F) resulting in a slight larger hydrodynamic radius compared to HFn, attributable to the steric hindrance of the PAS shell. Moreover, this analysis further confirms a single monodisperse

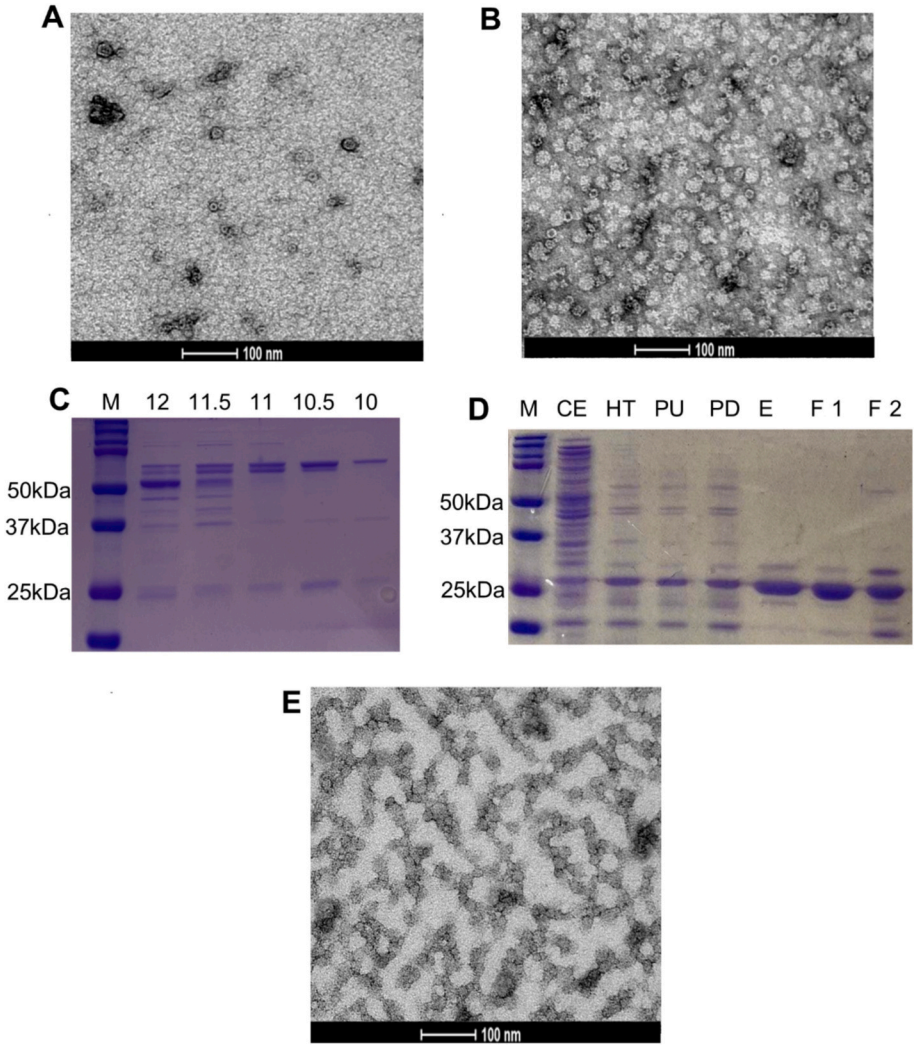

Fig. 4. Evaluation of factors influencing PAS20-HFn stability. A) TEM analysis of heat treated dialyzed sample (PD); B) TEM analysis of PD sample purified with SEC, using as elution buffer the same used for IEC (Tris-HCl 20 mM pH 8.0 supplemented with NaCl from 0.1 M to 0.3 M); C) SDS-PAGE 12 % (*v*/v) characterization of PAS20-HFn SEC run. M = molecular size marker. 4 μg of protein were loaded for all the fractions; D) SDS-PAGE 12 % (v/v) characterization of PAS20-HFn purified using DEAE-Sepharose resin. M = molecular size marker. 12 μg of protein were loaded for CE, HT, post ultracentrifuge (PU), and dialyzed sample (PD), whereas 4 μg of protein were loaded for excluded (E), fraction (F) 1 and 2. E) TEM analysis of PAS20-HFn purified with DEAE-Sepharose.

nanocage population in the solution and lack of protein aggregates.

CD analysis has been performed to gain further information on the secondary structure content of PAS20-HFn. As expected, CD spectra of PAS20-HFn compared with that of HFn (Fig. 5G) revealed a small shift in the first peak, which is attributable to an increase in random coil content. However, when we analyzed CD spectra, we observed some alterations between PAS20-HFn obtained by SEC *versus* IEC purification (Fig. S6; table S1), being the first assembled in nanocages and the last in monomers. PAS20-HFn spectra of nanocages achieved from SEC displayed a secondary content more similar to that observed for HFn, with the only exception of the increase in the unordered component. These observations further corroborate the idea that PAS20-HFn instability of quaternary structure is somehow intrinsic to the PAS20-HFn sequence and exacerbated by IEC. Indeed, PAS20-HFn is appropriately folded in nanocages by *E. coli* but loses its quaternary structure upon contact with the charged column resin. Moreover, CD data suggests that the loss of quaternary structure may be the result of some alterations in secondary structure, such as the increase in the helix 2 component highlighted.

3.5. Molecular modelling characterization of PAS20-HFn

To investigate the molecular behavior emerging during IEC purification, we studied the mutant structural properties using computational tools. Models were obtained by AlphaFold3 (AF3) server for native HFn, PAS20-HFn, PAS40-HFn dimers, tetramers, and octamers (see Fig. S7 for quality assessment of the top-scoring AF3 models).

The structure of the nanocage core, that is mostly constituted by the native sequence of HFn (Fig. S7A and S7D) was modelled with a high confidence based on the available structural data, while the models of the external region that corresponds to PAS domains was always poorly reliable (Figs. 6A and S7B, S7C and S7E), which is in agreement with the PAS sequence being disordered. The PAS20 and PAS40 domains are identical, except for the length of the PAS sequence. Indeed, PAS20-HFn displays a PAS sequence of 20 amino acids, while PAS40-HFn has two repetitions of the same PAS sequence, reaching a total of 40 amino acids. In order to gain insights into the dynamic properties of the disordered modification, we performed coarse-grain molecular dynamics (CG-MD) simulations taking advantage of the UNRES server. AF3 models of the native HFn, PAS20-HFn and PAS40-HFn dimers were used as a starting point for the generation of coarse-grained UNRES models, consisting of

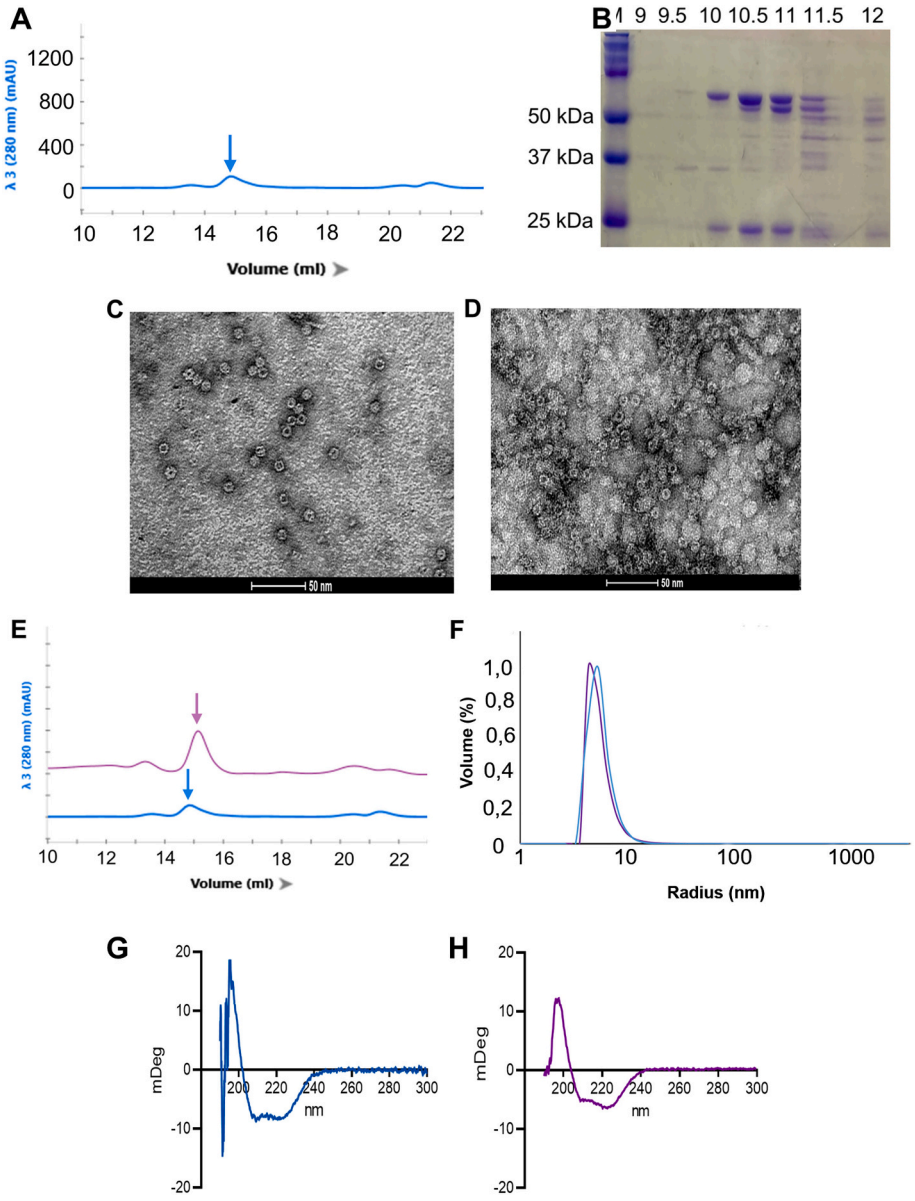

Fig. 5. PAS20-HFn characterization following purification by Size Exclusion Chromatography. A) FPLC chromatogram obtained with Superose 6 10/300 GL column. B) SDS-PAGE 12 % (*v*/v) characterization of PAS20-HFn purification. M = molecular size marker. 4 μg of protein were loaded for collected fractions. C) TEM analysis of purified PAS20-HFn and (D) HFn. E) Comparison between PAS20-HFn (blue) and HFn (violet) FPLC chromatograms obtained with Superose 6 10/300 GL column. F) DLS analysis of PAS20-HFn (blue) and HFn (violet). G) CD analysis of PAS20-HFn (blue) and (H) HFn (purple).

only two items for residue, one representing the Cα, nitrogen and oxygen atoms in the backbone of the protein, and the other representing the lateral chain of the residue. These models were submitted to a canonical CG-MD simulation for a maximum simulation time of 50 ns, obtaining 5 replicas for each system. The behavior of the dimer of the native HFn, the PAS20-HFn and the PAS40-HFn were not dissimilar and confirmed that the modified proteins are not unstable, despite a higher fluctuation of the Cα backbone in the PAS20-HFn N-terminal modification (calculated over the total time of simulation of the five replicas and the two chains in each dimer) (Figs. 6B, S8), likely due to its minor length.

Since no structural defects were evident for PAS20-HFn that could explain the low efficiency in building nanocages with this variant, we proceeded to investigate the behavior of the tetramers of HFn, PAS20-HFn, and PAS40-HFn with a similar approach. The CG-MD simulations were performed with five replicas starting from each of the AF3 models for each system (Fig. S9 for simulation radius of gyration and RMSD assessment). The characteristic behavior of the systems can be appreciated in Supplementary Videos S1, S2, and S3, which reproduce representative trajectories from the five replicas of each system. When the fluctuation of the Cα was calculated as an average over the four chains of the tetramer and the five replicas for each system, a peculiar property of the PAS20-HFn emerged (Fig. 6C). The fluctuation was very similar between HFn and PAS40-HFn, while PAS20-HFn showed higher flexibility in a region far from the PAS20 modification. This section is near to the extremely flexible C-terminal terminus and spans the region corresponding to aa 158–168 in the HFn depicted in Fig. 6D. This region involves the end of the D helix, the D-E turn and the beginning of the E helix, which are involved in building the interactions necessary for tetramer formation. Indeed, hydrophobic interactions between apolar residues in neighboring E helices and hydrogen bonds between main chain oxygen atoms contacts two subunits already forming a dimer with another HFn chain (thanks to a completely different interface along the A-B helices bundles), thus yielding the formation of a tetramer. These contacts allow further organization of higher order complexes, such as

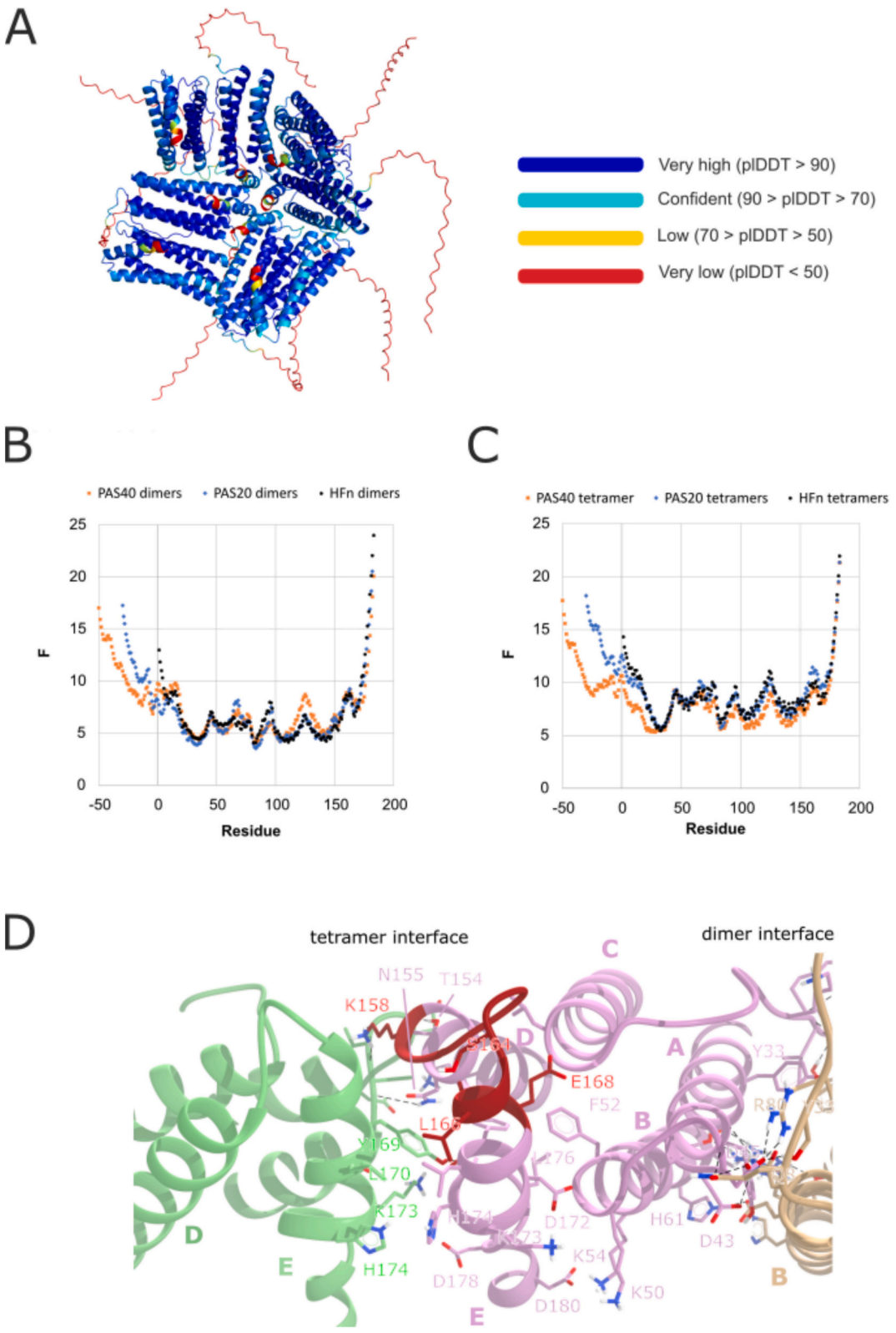

Fig. 6. PAS20 modifications interfere with the PAS20-HFn tetramer dynamic properties. A) Quality assessment of PAS20-HFn octamer built by AF3 and homology modelling. The parameter plDDT is shown as a gradient of color, according to the legend in the fig. B) Average fluctuation per residue calculated by 5 replicas CG-MD for HFn, PAS20-HFn, PAS40-HFn dimers. C) Average fluctuation per residue calculated by 5 replicas CG-MD for HFn, PAS20-HFn, PAS40-HFn tetramers. D) Interface involved in stabilizing the dimer of HFn and in the formation of a tetramer are indicated in the figure. The different chains are in differently colored cartoons. The fourth subunit is positioned under the green subunit and is not shown for improved clarity. Residues at the interface are shown as sticks. Capital letters indicate the helices A, B, C, D and E.

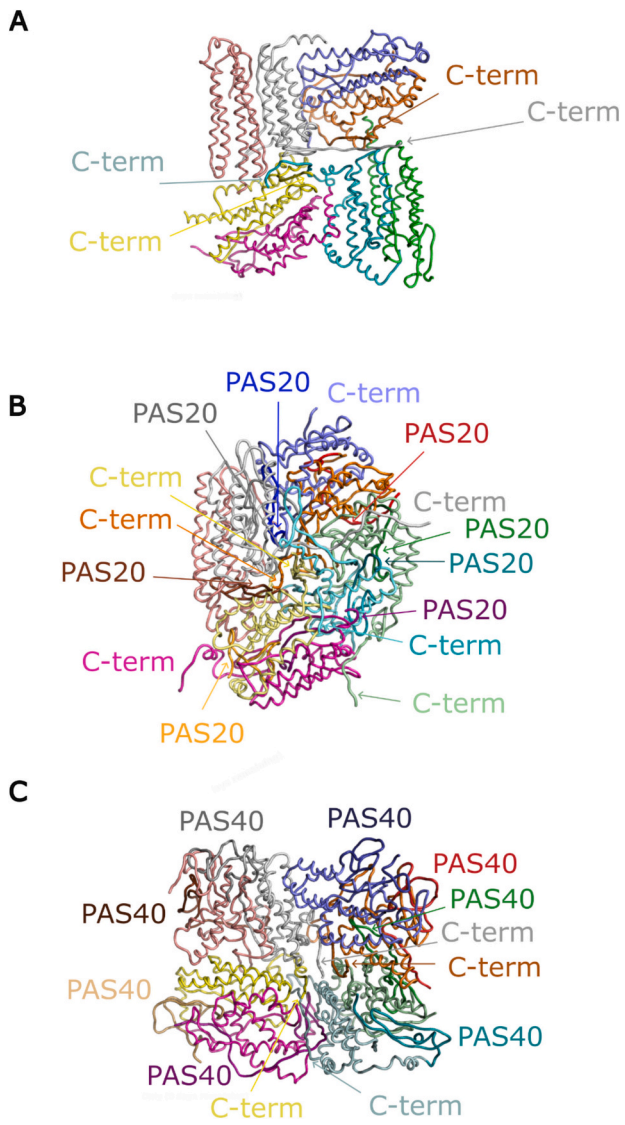

Fig. 7. PAS20 modifications interfere with the stability of the PAS20-HFn octamer. A) Structure of HFn (A), PAS20-HFn (B), and PAS40-HFn (C) octamer after CG-MD simulation. The different chains are in differently colored ribbons. The PAS20 and PAS40 modifications are highlighted in a darker shade.

an octamer of eight adjacent HFn subunits, organized in 4 dimers, arranged head to side (Fig. 7A), and finally the full 24-mer nanocage. The E helices of one subunit in each dimer in the 4-fold symmetry octamer protrude into the cavity, making a short, left-handed, four-helix bundle that is important to preserve the octamer symmetry (Fig. 7A).

Along the CG-MD simulation trajectory of wild-type HFn tetramer it is possible to observe that the aa 158–168 regions (marked in red in the Video S1), spanning the turn that connects D helix and E helix and control the dynamic behavior of the C-terminal E helix, keep the C-terminal regions of two of the four subunits close to each other. During the CG-MD simulation of PAS20-HFn tetramers, the behavior of these regions is completely different due to the interference of the PAS20 regions. In detail, the PAS20 N-terminal modifications interact with the proximal subunits' modifications and C-terminal regions themselves, disrupting the correct association of the C-terminal *E*-helices (Video S2). This behavior is only rarely observed during the CG-MD simulations of PAS40-HFn tetramers (Video S3), since the PAS40 modifications generally assume a self-interacting structure that limits the interference with the adjacent subunits.

In order to evaluate the possible effects of this aberrant behavior in PAS20-HFn, we performed CG-MD simulations starting from the top two scoring models generated by AF3 for HFn and PAS40-HFn octamers (Fig. S10 for simulation radius of gyration and RMSD assessment). As far as PAS20-HFn octamers are concerned, AF3 was for unknown reasons not able to generate any 4-axis symmetry octamer model but only a 3-axis symmetry model with the fourth dimer interacting with only one of the other dimers. In order to obtain the 4-axis symmetric octamer, we decided to proceed by homology modelling and repositioned the misaligned dimer. The original model from AF3 and the 4-axis symmetric model were both submitted to CG-MD simulations, revealing similar properties of the PAS20-HFn complexes. In detail, while the four E helices bundle was flexible but recognizable during the simulation of native HFn (Video S4 and Fig. 7A), the interaction of the C-terminal regions in PAS20-HFn octamers was disturbed by the asymmetric behavior of the subunits driven by the interference of the PAS20 modifications of one subunit with the adjacent subunits (Video S5 and Fig. 7B). This behavior is much less evident during PAS40-HFn octamers simulation (Video S6 and Fig. 7C), where the PAS40 modifications dock on the same subunits and do not interfere with the interaction surfaces involved in the complex assembly.

3.6. Functional alterations of PAS20-HFn

To elucidate if the alteration in PAS20-HFn nanocage formation may impact on PAS20-HFn functionality, we decided to assess the PAS cleavage, tumor recognition and nanodrug development. Starting from cleavage results achieved with PAS40-HFn, we performed a cleavage assay incubating PAS20-HFn nanocages with Collagenase I at 37 °C. Using the Collagenase I: PAS20-HFn ratio of 1:4, we didn't observe PAS removal (data not shown). To achieve the full cleavage of PAS20 domains from PAS20-HFn nanocage, we had to increase the ratio to 1:2 and the incubation time up to 120 h. Unexpectedly, if we perform the same experiment using PAS20-HFn monomers unable to fold into a nanocage structure, we observe that collagenase I is completely unable to cleave the PAS20 domain (Fig. 8A). These results, when compared with those achieved with PAS40-HFn, underline another important functional alteration that makes PAS20-HFn unsuitable as delivery system.

If we consider the PAS20-HFn and PAS40-HFn nanocages' binding (Fig. 8B), we observed a similar behavior. Both nanocages displayed lower binding in comparison to native HFn, as expected due to the presence of the PAS shell. Consistently, when PAS domains were removed, the full binding capability was restored. These results strongly indicate that, when the nanocage is correctly folded, PAS20-HFn instability didn't affect cancer cells binding. Different outcomes should be awaited about drug or dye loading inside HFn nanocages, since we expected PAS20-HFn instability to dramatically impact the loading process. Indeed, it is impossible to achieve the same amount of drug or dye encapsulated without a functional nanocage. Different loading procedures are available, displaying different degrees of aggressiveness to the nanocage structure [32]. In order to characterize PAS20-HFn functionality, we decided to test one of the strongest methods: the pH-mediated disassembly-reassembly. This procedure is only partially reversible, and should definitively prove if the PAS20 domain affects PAS20-HFn stability. We chose the fluorescent dye ICG, as cargo molecule. As we can see in the Table 3, the loading procedure performed with PAS20-HFn nanocages results in about one order of magnitude decrease of encapsulated ICG, coupled with a strongly reduced recovery.

4. Conclusions

This work presents a comprehensive study of how surface functionalization with a short PAS sequence affects the stability of HFn nanocages. It introduces a novel perspective on the impact of PASylation of HFn, clearly demonstrating for the first time in literature its bipolar and crucial role, particularly in relation to its size. While it is widely

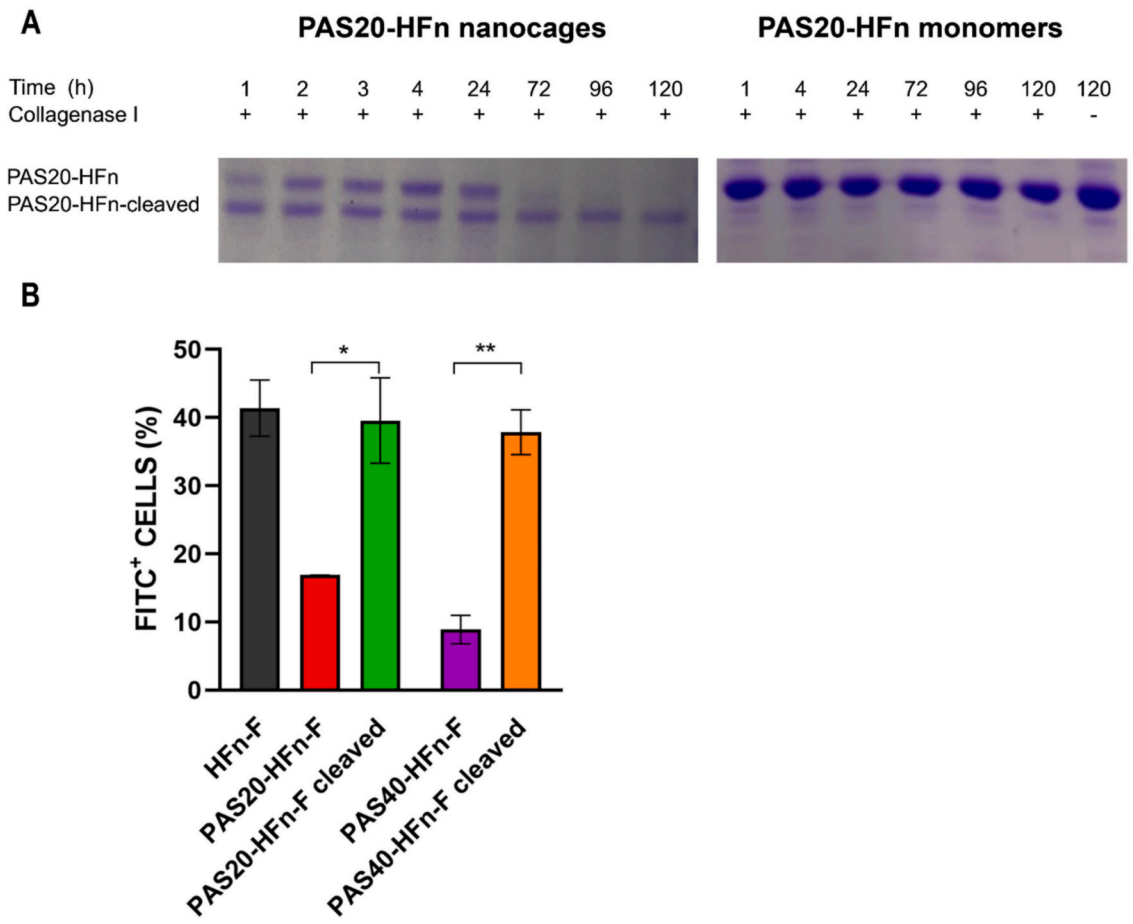

Fig. 8. PAS20-HFn functional alterations. A) SDS-PAGE analysis of PAS20 domain cleavage. PAS20-HFn nanocages and monomers loaded in a 12 % (*v*/v) SDS-PAGE stained with Coomassie blue at different times after Collagenase I incubation. M = molecular weight marker. B) Binding assay of FITC-labelled PAS40-HFn, PAS20-HFn and native HFn. 4T1 cells were incubated before and after Collagenase I cleavage with 100 μg/mL of PAS20-HFn-F (red and green, respectively) and PAS40-HFn-F (violet and orange, respectively). Native HFn (dark grey) has been used as a positive control, while untreated cells have been used to set the positive region and the singlet gate. Data are reported as average ± S.D. of two independent experiments and expressed as a percentage of cells in the positive region to HFn−FITC fluorescence. One-way ANOVA statistical significance: $*p < 0.05$; $**p < 0.01$.

Table 3
Summary of the amount of ICG loaded andofpercentage of recovery in PAS40-HFn, PAS20-HFn and HFn. Replicates = n. Statistical significance *vs* HFn@ICG (CTRL): **p < 0.01; n.s. $p > 0.05$.

	PAS40-HFn@ICG	PAS20-HFn@ICG	HFn@ICG
ICG encapsulated (mg)	1.50 ± 0.67; n.s.	0.22 ± 0.06; **	1.29 ± 0.31
% recovery	26.66 ± 7.52; n.s	1.08 ± 0.31; **	31.07 ± 7.87
n	3	2	3

recognized that PASylation may significantly enhance protein stabilization, no negative contributions had been reported until now. Results obtained from comparing two PASylated variants of HFn -one containing a short random coil PAS sequence of 20 amino acids (PAS20-HFn) and the other with two repeats of the same sequence (PAS40-HFn) – both preserving the folding of HFn domain folding, strongly revealed the crucial role of PAS domain size in maintaining the functionality of HFn nanocages. Moreover, this study emphasizes the importance of not only performing structural modelling of new HFn mutants, but also gaining insights into PAS domain interactions by molecular dynamic simulations. To date, this research does not provide direct insight into the molecular mechanism by which PAS20 disrupts HFn oligomerization, an area that warrants future explorations. In a nutshell, these findings contribute to decipher how the surface functionalization can critically impact the stability of HFn nanocages, paving the way for future studies on functionalization.

Supporting tables including secondary structure content analysis of HFn, PAS20-HFn and PAS40-HFn as determined by DichroWeb using the CONTIN-LL algorithm and SP175t reference set (Table S1). Additional analyses including induction tests of PAS20-HFn (Fig. S1) and PAS40-HFn (Fig. S2), PAS40-HFn characterization following Ion Exchange Chromatography (Fig. S3), DLS analysis of PAS20-HFn purified using Ion Exchange Chromatography (Fig. S4), CD overlay analysis of PAS20-HFn purified using Ion Exchange Chromatography and PAS20-HFn purified using Size Exclusion Chromatography (Fig. S5), Quality assessment of the top scoring models of HFn, PAS20-HFn, and PAS40-HFn octamers generated by Alphafold3 (Fig. S6), Root Mean Square Deviation for HFn, PAS20-HFn and PAS40-HFn dimers (Fig. S7), tetramers (Fig. S8), octamers (Fig. S9) CG-MD simulations. Supplementary Videos including Dynamics properties of HFn tetramer (Video S1), Dynamics properties of PAS20-HFn tetramer (Video S2), Dynamics properties of PAS40-HFn tetramer (Video S3), Dynamics properties of HFn octamer (Video S4), Dynamics properties of PAS20-HFn octamer (Video S5), Dynamics properties of PAS40-HFn octamer (Video S6). Supplementary data to this article can be found online at https://doi.org/10.1016/j.ijbiomac.2025.147809.

CRediT authorship contribution statement

Ilaria Tagliolini: Writing – review & editing, Writing – original

draft, Investigation, Formal analysis. **Francesca Gorgoglione:** Writing – review & editing, Methodology. **Marta Sevieri:** Writing – review & editing, Methodology, Investigation, Formal analysis. **Beatrice Bignami:** Writing – review & editing, Writing – original draft, Methodology, Investigation, Formal analysis. **Valeria Giacobbo:** Writing – review & editing, Methodology, Investigation. **Claudia Pigliacelli:** Writing – review & editing, Methodology. **Fabio Corsi:** Writing – review & editing, Methodology. **Renata Tisi:** Writing – review & editing, Writing – original draft, Methodology, Investigation, Formal analysis. **Serena Mazzucchelli:** Writing – review & editing, Writing – original draft, Supervision, Funding acquisition, Conceptualization.

Informed consent statement

Not applicable.

Institutional review board statement

Not applicable.

Funding

The research leading to these results has received funding from AIRC under IG2022-ID27107 P.I Mazzucchelli.

Declaration of competing interest

The authors declare no conflict of interest.

Acknowledgments

We acknowledge AIRC IG2022-ID27107 P.I Mazzucchelli for V.G. and M.S. post-doctoral position.

Data availability

Data available in a publicly accessible repository upon request at https://doi.org/10.13130/RD_UNIMI/OQPPLU.

References

[1] S. Gupta, R. Kaur, A. Bhardwaj, D. Parashar, Multifunctional nanomaterials: recent advancements in cancer therapeutics and vaccines, Indian J. Microbiol. 65 (1) (2024) 51–68, https://doi.org/10.1007/s12088-024-01274-x.

[2] F. Mainini, A. Bonizzi, M. Sevieri, L. Sitia, M. Truffi, F. Corsi, S. Mazzucchelli, Protein-based nanoparticles for the imaging and treatment of solid tumors: the case of ferritin nanocages, a narrative review, Pharmaceutics 13 (2021) 2000, https://doi.org/10.3390/pharmaceutics13122000.

[3] M.A. Rizzuto, R. Dal Magro, L. Barbieri, L. Pandolfi, A. Sguazzini-Viscontini, M. Truffi, L. Salvioni, F. Corsi, M. Colombo, F. Re, D. Prosperi, H-ferritin nanoparticle-mediated delivery of antibodies across a BBB in vitro model for treatment of brain malignancies, Biomater. Sci. 9 (6) (2021) 2032–2042, https://doi.org/10.1039/d0bm01726d.

[4] X. Cheng, K. Fan, L. Wang, X. Ying, A.J. Sanders, T. Guo, X. Xing, M. Zhou, H. Du, Y. Hu, H. Ding, Z. Li, X. Wen, W. Jiang, X. Yan, J. Ji, TfR1 binding with H-ferritin nanocarrier achieves prognostic diagnosis and enhances the therapeutic efficacy in clinical gastric cancer, Cell Death Dis. 11 (2) (2020), https://doi.org/10.1038/s41419-020-2272-z.

[5] C.J. Greene, K. Attwood, N.J. Sharma, K.W. Gross, G.J. Smith, B. Xu, E. C. Kauffman, Transferrin receptor 1 upregulation in primary tumor and downregulation in benign kidney is associated with progression and mortality in renal cell carcinoma patients, Oncotarget 8 (63) (2017) 107052–107075, https://doi.org/10.18632/oncotarget.22323.

[6] C. Chen, P. Liu, X. Duan, M. Cheng, L.X. Xu, Deferoxamine-induced high expression of TfR1 and DMT1 enhance iron uptake in triple-negative breast cancer cells by activating IL-6/PI3K/Akt pathway, Onco. Targets Ther. 12 (2019) 4359–4377, https://doi.org/10.2147/OTT.S193507.

[7] B. Jiang, L. Fang, K. Wu, X. Yan, F. Kelong, Ferritins as natural and artificial nanozymes for theranostics, Theranostics 10 (2) (2020) 687–706, https://doi.org/10.7150/thno.39827.

[8] Z. Wang, Y. Zhao, S. Zhang, X. Chen, G. Sun, B. Zahng, B. Jiang, Y. Yang, X. Yan, K. Fan, Re-engineering the inner surface of ferritin nanocage enables dual drug payloads for synergistic tumor therapy, Theranostics 12 (4) (2022) 1800–1815, https://doi.org/10.7150/thno.68459.

[9] K. Fan, C. Cao, Y. Pan, D. Lu, D. Yang, J. Feng, L. Song, M. Liang, X. Yan, Magnetoferritin nanoparticles for targeting and visualizing tumour tissues, Nat. Nanotechnol. 7 (7) (2012) 459–464, https://doi.org/10.1038/nnano.2012.90.

[10] X. Song, Y. Zheng, L. Zhu, L. Zhang, H. Meng, R. Yu, C. Zhang, Development of robust and facile purification process for production of recombinant human ferritin heavy chain nanoparticle from *Escherichia coli*, Process Biochem. 104 (2021) 1–9, https://doi.org/10.1016/j.procbio.2021.02.014.

[11] M. Sevieri, C. Sottani, A. Chesi, A. Bonizzi, L. Sitia, F.S. Robustelli Della Cuna, E. Grignani, F. Corsi, S. Mazzucchelli, Deciphering the role of H-ferritin nanocages in improving tumor-targeted delivery of Indocyanine green: combined analysis of murine tissue homogenates with UHPLC–MS/MS and fluorescence, ACS Omega 8 (51) (2023) 48735–48741, https://doi.org/10.1021/acsomega.3c05566.

[12] Y. Shen, X. Li, D. Dong, B. Zhang, Y. Xue, P. Shang, Transferrin receptor 1 in cancer: a new sight for cancer therapy, Am. J. Cancer Res. 8 (6) (2018) 916–931.

[13] P.J. Thul, C. Lindskog, The human protein atlas: a spatial map of the human proteome, Protein Sci. 27 (2018) 233–244, https://doi.org/10.1002/pro.3307.

[14] S. Mazzucchelli, M. Bellini, L. Fiandra, M. Truffi, M.A. Rizzuto, L. Sorrentino, E. Longhi, M. Nebuloni, D. Prosperi, F. Corsi, Nanometronomic treatment of 4T1 breast cancer with nanocaged doxorubicin prevents drug resistance and circumvents cardiotoxicity, Oncotarget 8 (5) (2017) 8383–8396, https://doi.org/10.18632/oncotarget.14204.

[15] A. Bonizzi, M. Truffi, M. Sevieri, R. Allevi, L. Sitia, R. Ottria, L. Sorrentino, C. Sottani, S. Negri, E. Grignani, S. Mazzucchelli, F. Corsi, Everolimus nanoformulation in biological nanoparticles increases drug responsiveness in resistant and low-responsive breast cancer cell lines, Pharmaceutics 11 (2019) 384, https://doi.org/10.3390/pharmaceutics11080384.

[16] M. Sevieri, L. Sitia, A. Bonizzi, M. Truffi, S. Mazzucchelli, F. Corsi, Tumor accumulation and off-target biodistribution of an indocyanine-green fluorescent nanotracer: an ex vivo study on an orthotopic murine model of breast cancer, Int. J. Mol. Sci. 22 (4) (2021) 1–12, https://doi.org/10.3390/IJMS22041601.

[17] F. Andreata, A. Bonizzi, M. Sevieri, M. Truffi, M. Monieri, L. Sitia, F. Silva, L. Sorrentino, R. Allevi, P. Zerbi, B. Marchini, E. Longhi, R. Ottria, S. Casati, R. Vanna, C. Morasso, M. Bellini, D. Prosperi, F. Corsi, S. Mazzucchelli, Co-administration of H-ferritin-doxorubicin and Trastuzumab in neoadjuvant setting improves efficacy and prevents cardiotoxicity in HER2 + murine breast cancer model, Sci. Rep. 10 (1) (2020), https://doi.org/10.1038/s41598-020-68205-w.

[18] S. Mazzucchelli, M. Truffi, F. Baccarini, M. Beretta, L. Sorrentino, M. Bellini, M. A. Rizzuto, R. Ottria, A. Ravelli, P. Ciuffreda, D. Prosperi, F. Corsi, H-ferritin-nanocaged olaparib: a promising choice for both BRCA-mutated and sporadic triple negative breast cancer, Sci. Rep. 7 (1) (2017), https://doi.org/10.1038/s41598-017-07617-7.

[19] M. Sevieri, F. Andreata, F. Mainini, L. Signati, F. Piccotti, M. Truffi, A. Bonizzi, L. Sitia, C. Pigliacelli, C. Morasso, B. Tagliaferri, F. Corsi, S. Mazzucchelli, Impact of doxorubicin-loaded ferritin nanocages (FerOX) vs. free doxorubicin on T lymphocytes: a translational clinical study on breast cancer patients undergoing neoadjuvant chemotherapy, J. Nanobiotechnol. 22 (1) (2024), https://doi.org/10.1186/s12951-024-02441-4.

[20] L. Sitia, M. Sevieri, A. Bonizzi, R. Allevi, C. Morasso, D. Foschi, F. Corsi, S. Mazzucchelli, Development of tumor-targeted indocyanine green-loaded ferritin nanoparticles for intraoperative detection of cancers, ACS Omega 5 (21) (2020) 12035–12045, https://doi.org/10.1021/acsomega.0c00244.

[21] L. Sitia, C. Sottani, P. Saccomandi, L. Bianchi, M. Sevieri, R. Allevi, E. Grignani, S. Mazzucchelli, F. Corsi, Combined ferritin nanocarriers with ICG for effective phototherapy against breast cancer, Int. J. Nanomedicine 19 (2024) 4263–4278, https://doi.org/10.2147/ijn.s445334.

[22] M. Bellini, S. Mazzucchelli, E. Galbiati, S. Sommaruga, L. Fiandra, M. Truffi, M. A. Rizzuto, M. Colombo, P. Tortora, F. Corsi, D. Prosperi, Protein nanocages for self-triggered nuclear delivery of DNA-targeted chemotherapeutics in cancer cells, J. Control. Release 196 (2014) 184–196, https://doi.org/10.1016/j.jconrel.2014.10.002.

[23] M. Sevieri, M. Pinori, A. Chesi, A. Bonizzi, L. Sitia, M. Truffi, C. Morasso, F. Corsi, S. Mazzucchelli, Novel bioengineering strategies to improve bioavailability and in vivo circulation of H-ferritin nanocages by surface functionalization, ACS Omega 8 (8) (2023) 7244–7251, https://doi.org/10.1021/acsomega.2c07794.

[24] E. Falvo, F. Malagrinò, A. Arcovito, F. Fazi, G. Colotti, E. Tremante, P. Di Micco, A. Braca, R. Opri, A. Giuffrè, G. Fracasso, P. Ceci, The presence of glutamate residues on the PAS sequence of the stimuli-sensitive nano-ferritin improves in vivo biodistribution and mitoxantrone encapsulation homogeneity, J. Control. Release 275 (2018) 177–185, https://doi.org/10.1016/j.jconrel.2018.02.025.

[25] G. Fracasso, E. Falvo, G. Colotti, F. Fazi, T. Ingegnere, A. Amalfitano, G. B. Doglietto, S. Alfieri, A. Boffi, V. Morea, G. Conti, E. Tremante, P. Giacomini, A. Arcovito, P. Ceci, Selective delivery of doxorubicin by novel stimuli-sensitive nano-ferritins overcomes tumor refractoriness, J. Control. Release 239 (2016) 10–18, https://doi.org/10.1016/j.jconrel.2016.08.010.

[26] M. Schlapschy, U. Binder, C. Börger, I. Theobald, K. Wachinger, S. Kisling, D. Haller, A. Skerra, PASylation: a biological alternative to PEGylation for extending the plasma half-life of pharmaceutically active proteins, Protein Eng. Des. Sel. 26 (8) (2013) 489–501, https://doi.org/10.1093/protein/gzt023.

[27] E. Falvo, E. Tremante, A. Arcovito, M. Papi, N. Elad, A. Boffi, V. Morea, G. Conti, G. Toffoli, G. Fracasso, P. Giacomini, P. Ceci, Improved doxorubicin encapsulation and pharmacokinetics of ferritin-fusion protein nanocarriers bearing PAS elements, Biomacromolecules 17 (2016) 514–522, https://doi.org/10.1021/acs.biomac.5b01446.

[28] U. Binder, A. Skerra, PASylation®: a versatile technology to extend drug delivery, Curr. Opin. Colloid Interface Sci. 31 (2017) 10–17, https://doi.org/10.1016/j.cocis.2017.06.004.
[29] A.J. Miles, S.G. Ramalli, B.A. Wallace, DichroWeb, a website for calculating protein secondary structure from circular dichroism spectroscopic data, Protein Sci. 31 (1) (2022) 37–46, https://doi.org/10.1002/pro.4153.
[30] R. Ślusarz, E.A. Lubecka, C. Czaplewski, A. Liwo, Improvements and new functionalities of UNRES server for coarse-grained modeling of protein structure, dynamics, and interactions, Front. Mol. Biosci. 9 (2022), https://doi.org/10.3389/fmolb.2022.1071428.
[31] C. Czaplewski, A. Karczynska, A.K. Sieradzan, A. Liwo, UNRES server for physics-based coarse-grained simulations and prediction of protein structure, dynamics and thermodynamics, Nucleic Acids Res. 46 (W1) (2018) W304–W309, https://doi.org/10.1093/nar/gky328.
[32] J. Zhang, D. Cheng, J. He, J. Hong, C. Yuan, M. Liang, Cargo loading within ferritin nanocages in preparation for tumor-targeted delivery, Nat. Protoc. 16 (10) (2021) 4878–4896, https://doi.org/10.1038/s41596-021-00602-5.